

This is an Open Access document downloaded from ORCA, Cardiff University's institutional repository: <https://orca.cardiff.ac.uk/id/eprint/106675/>

This is the author's version of a work that was submitted to / accepted for publication.

Citation for final published version:

He, Qian , Sun, Mingzi, Kuang, Xiao-jun, Huang, Bolong, Ye, Shi and Zhang, Qin-yuan 2017. Unraveling the correlation between oxide-ion motion and upconversion luminescence in $\text{bLa}_2\text{Mo}_2\text{O}_9:\text{Yb}^{3+},\text{Er}^{3+}$ derivatives. *Journal of Materials Chemistry C* 5 (42) , pp. 10965-10970. 10.1039/C7TC03695G

Publishers page: <http://dx.doi.org/10.1039/C7TC03695G>

Please note:

Changes made as a result of publishing processes such as copy-editing, formatting and page numbers may not be reflected in this version. For the definitive version of this publication, please refer to the published source. You are advised to consult the publisher's version if you wish to cite this paper.

This version is being made available in accordance with publisher policies. See <http://orca.cf.ac.uk/policies.html> for usage policies. Copyright and moral rights for publications made available in ORCA are retained by the copyright holders.



Unraveling the correlation between oxide-ion motion and upconversion luminescence in b-La₂Mo₂O₉:Yb³⁺,Er³⁺ derivatives†

Qian He,^a Mingzi Sun,^b Xiao-jun Kuang,^c Bolong Huang,^b Shi Ye^{*a} and Qin-yuan Zhang^a

An optical approach is an alternative method to give insight into the oxide-ion motion in oxide-ion conductors. Herein, we illustrate the correlation between upconversion (UC) luminescence in Yb³⁺-Er³⁺ and oxide-ion motion in a b-La₂(Mo,W)₂O₉ series. The break points at B150 1C in the logarithmic UC emission intensity ratio of I₅₂₅/I₆₆₀ or I₆₆₀/I₅₅₀ (the three emission peaks of Er³⁺) versus temperature imply oxide-ion jumps, whereas the slopes of these plots above 150 1C suggest the capacity of oxide-ion motion. Specifically, the larger the absolute slope values, the higher the oxide-ion conduction capacity. Due to the pinning feature of the Fermi level contributed by the Mo-O bonds in b-La₂Mo₂O₉ both with and without anion-Frenkel defects or W dopants, as revealed by density functional theory calculations, b-La₂Mo₂O₉ remains electronically insulating. Thus, the increase in activation energy and decline in conductivity with an increase in W contents at low temperature (<400 1C) are likely attributed to the higher barrier for the formation of new anion-Frenkel defects. This research gives another perspective on oxide-ion conductors via an optical probe.

Introduction

Oxide-ion conductors are essential for clean electrochemical applications not only in solid oxide fuel cells, but also in oxygen sensors and oxygen separation.¹⁻³ Therefore, it is necessary to investigate the thermally driven oxide-ion motion and to understand the long-range oxide-ion conductivity in oxide-ion conductors. A previous report⁴ suggested an optical approach to detect oxide-ion swapping in a-La₂Mo₂O₉ in addition to all the available approaches such as internal friction spectroscopy,⁵ neutron powder diffraction^{6,7} and simulation,⁸ which utilizes the upconversion (UC) luminescence intensity ratio of the ²H_{11/2}, ⁴S_{3/2}, ⁴F_{9/2} - ⁴I_{15/2} transitions of Er³⁺. An internal reference with the intensity ratio of ²H_{11/2} - ⁴I_{15/2} to ⁴S_{3/2} - ⁴I_{15/2} transitions, which is independent of luminescence loss and fluctuations in excitation intensity and thus varies linearly with temperature,

was used to verify the method. Moreover, this is proven by the fact that the green emission of ²H_{11/2} - ⁴I_{15/2} is much more sensitive to variations in the crystallographic site of Er³⁺ (related to the Judd-Ofelt intensity parameter O₂), whereas the red emission of ⁴F_{9/2} - ⁴I_{15/2} of Er³⁺ is hardly affected but more sensitive to O₄ and O₆.⁹⁻¹⁴ However, more information on the correlation between UC luminescence and capacity of oxide-ion motion in this system is needed.

La₂Mo₂O₉ is an outstanding oxide-ion conductor due to the high concentration of intrinsic oxygen vacancies embedded in its crystal lattice, which was first reported by Lacorre et al.³ This material undergoes a phase transition from the a-form to the b-form at 580 1C, which is accompanied by an increase in conductivity of almost 2 orders of magnitude.^{3,15-17} b-La₂Mo₂O₉ has a cubic structure with the space group P2₁3, which is analogous to the structure of b-SnWO₄ based on the so-called lone pair substitution (LPS) concept.^{3,5,18} Specifically, Sn²⁺ with a lone pair is non-equivalent substituted by La³⁺ and O(3),¹⁹ which increases the concentration of intrinsic oxygen vacancies and provides abundant paths for the diffusion of oxide ions. This results in the high ionic conductivity of b-La₂Mo₂O₉.²⁰ Its high oxide-ion conductivity can also be primarily ascribed to the flexibility of MoO_x (x = 4, 5 and 6)^{4,21} and anion-Frenkel (a-Fr) defects.²² There are reports that substitution by other ions at either the La sites or Mo sites in La₂Mo₂O₉ can suppress the phase transition, which stabilizes the high-temperature cubic

^aState Key Lab of Luminescent Materials and Devices, and Guangdong Provincial Key Laboratory of Fiber Laser Materials and Applied Techniques, South China University of Technology, Guangzhou 510641, China. E-mail: msyes@scut.edu.cn

^bDepartment of Applied Biology and Chemical Technology, The Hong Kong Polytechnic University, Hung Hom, Kowloon, Hong Kong SAR, China. E-mail: bolong.huang@polyu.edu.hk

^cGuangxi Ministry-Province Jointly-Constructed Cultivation Base for State Key Laboratory of Processing for Nonferrous Metal and Featured Materials, College of Materials Science and Engineering, Guilin University of Technology, Guilin 541004, China

† Electronic supplementary information (ESI) available. See DOI: 10.1039/c7tc03695g

b-La₂Mo₂O₉ structure at room temperature.^{3,6,16,23–26} According to previous research, substitution of Mo⁶⁺ by W⁶⁺ can stabilize the b phase at room temperature.^{7,20,22,27} W⁶⁺ substitution inevitably influences both oxide ion conductivity and electronic conductivity, which conversely impose distinct effects on the UC luminescence of Yb³⁺–Er³⁺. Therefore, it would be beneficial to determine the dominant effect of W substitution on the thermally driven oxide-ion motion via luminescent/conductive measurements and density functional theory (DFT) calculations since DFT calculations on electronic structure may give some insight. Thus, this research focuses on La₂(Mo,W)₂O₉:Yb³⁺,Er³⁺ with the assistance of temperature-dependent UC emission spectroscopy, Raman spectroscopy, alternating current (AC) impedance spectroscopy, and DFT calculations.

Experimental

La_{1.9}Yb_{0.06}Er_{0.04}Mo_{2-x}W_xO₉ (x = 0, 0.25, 0.75 and 1.25) was synthesized through a traditional solid state reaction according to Fournier et al.²⁸ Typically, stoichiometric amounts of La₂O₃ (99.99%), MoO₃ (analytical reagent, A.R.), WO₃ (A.R.), Yb₂O₃ (99.99%) and Er₂O₃ (99.99%) were mixed thoroughly in an agate mortar. The mixture was first calcined at 500 °C for 10 h and then at 970 °C for 13 h with intermediate grinding. Sintered ceramics were prepared using the mixed raw materials presintered at 500 °C for 10 h as precursors. Then, the precursors were thoroughly mixed with polyvinyl alcohol (PVA) binder solution and pressed under 20 MPa pressure into pellets. Finally, the pellets were sintered at 970 °C for 13 h in air. The sintered ceramic pellets for electric testing were B1 mm in thickness and B10 mm in diameter. The phase purity of the ceramics was identified via powder X-ray diffraction (XRD) (Philips PW1830) with a graphite monochromator and Cu K α irradiation. UC emission spectra were recorded on a Horiba JOBIN YVON iHR 320 spectrofluorometer equipped with a R928 photomultiplier tube as the detector. The excitation light source was a 980 nm laser diode (LD, Coherent Corp.) for the UC measurement. Temperature-dependent luminescence behaviors were measured using a TAP-02 high-temperature fluorescence accessory (Tian Jin Orient-KOJI instrument Co., Ltd, China). AC impedance spectroscopy measurements were performed with a Solatron 1260 Impedance/Gain-Phase Analyzer over the frequency range of 0.1–10⁷ Hz from room temperature to 650 °C in air. Prior to the measurement, gold was pasted on both sides of the ceramic pellets and then heated at 550 °C for 40 min in air to obtain the electrodes.²⁹

For the electronic structure calculations of the W-doped La₂Mo₂O₉ with anion(oxide-ion)-Frenkel (a-Fr) pair defects, ultrafine quality and ultrasoft pseudopotentials with a plane-wave cutoff energy of 380 eV were chosen in the CASTEP software package. Reciprocal space integration was performed using Monkhorst–Pack k-point grids of 2 2 2 k-points in the Brillouin zone. The calculations used tolerance settings as follows: total energy lower than 5.0 10⁻⁴ eV per atom and maximum ionic Hellmann–Feynman force lower than 0.1 eV Å⁻¹.

Regarding the geometry relaxation, the Broyden–Fletcher–Goldfarb–Shanno (BFGS) algorithm method was used for all doping and defect supercell calculations.

Results and discussion

XRD patterns and Raman spectroscopy

Fig. 1a presents the room temperature XRD patterns of the La₂Mo_{2-x}W_xO₉ (x = 0.25, 0.75 and 1.25) samples and the standard XRD patterns of cubic b-La₂Mo₂O₉ (ICSD98871). The inset of Fig. 1a is the enlarged pseudo-cubic (231) diffraction line. It is reported that monoclinic a-La₂Mo₂O₉ has several splitting peaks for the pseudo-cubic reflection (231) at around 2 θ = 46–49 $^{\circ}$;^{24,25} however, the peaks in the inset appear to be different from that of monoclinic a-La₂Mo₂O₉.

Raman spectroscopy is a powerful tool to give supporting evidence for the b-La₂Mo₂O₉ structure.^{7,17,25,26} Fig. 1b shows Raman spectra for La₂Mo_{2-x}W_xO₉ (x = 0, 0.25, 0.75 and 1.25) at room temperature. The band at 700–1000 cm⁻¹ gives information about the structure transformation.²⁶ There should be a significant change in the structure of b-La₂Mo₂O₉ since there are only two apparent peaks, while for the a-La₂Mo₂O₉ phase there are at least four apparent distinguished peaks. The two peaks at around 869 cm⁻¹ (peak 1) and 922 cm⁻¹ (peak 2) are broadened or diminished with W doping, which indicates that the doped samples are in the b form.^{17,30} Thus, the cubic structure is stabilized by doping W, which is similar to that in the previous

research.^{7,16,17,24–26,31,32}

Temperature-dependent UC behaviors and AC impedance spectroscopy

All the samples exhibit bright and shining UC luminescence at room temperature upon excitation with a 980 nm diode laser. The typical UC emission spectra of La_{1.9}Yb_{0.06}Er_{0.04}Mo_{1.75}W_{0.25}O₉ recorded at different temperatures are illustrated in Fig. 2a. The green emission peaks at B525 nm and B550 nm are attributed to ²H_{11/2} - ⁴I_{15/2} and ⁴S_{3/2} - ⁴I_{15/2}, respectively, whereas the red emission peak at B660 nm is ascribed to the ⁴F_{9/2} - ⁴I_{15/2} transitions of Er³⁺. The temperature-dependent UC emission spectra of the other La_{1.9}Yb_{0.06}Er_{0.04}Mo_{2-x}W_xO₉ (x = 0.75 and 1.25) samples are similar to that of La_{1.9}Yb_{0.06}Er_{0.04}Mo_{1.75}W_{0.25}O₉. Fig. 2b presents the spectra normalized at the B550 nm peak, in

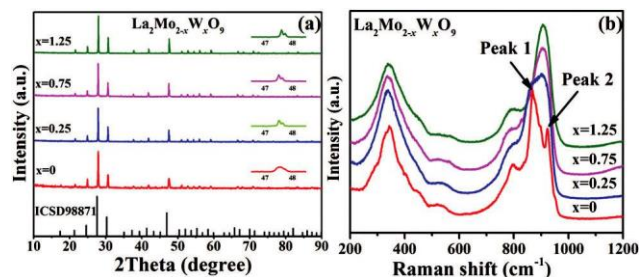


Fig. 1 (a) XRD patterns of the La₂Mo_{2-x}W_xO₉ (x = 0.25, 0.75 and 1.25) samples recorded at room temperature, together with the reference of cubic b-La₂Mo₂O₉ (ICSD98871), inset: enlarged pseudo-cubic (231) peaks. (b) Raman spectra for La₂Mo_{2-x}W_xO₉ (x = 0, 0.25, 0.75 and 1.25) at room temperature.

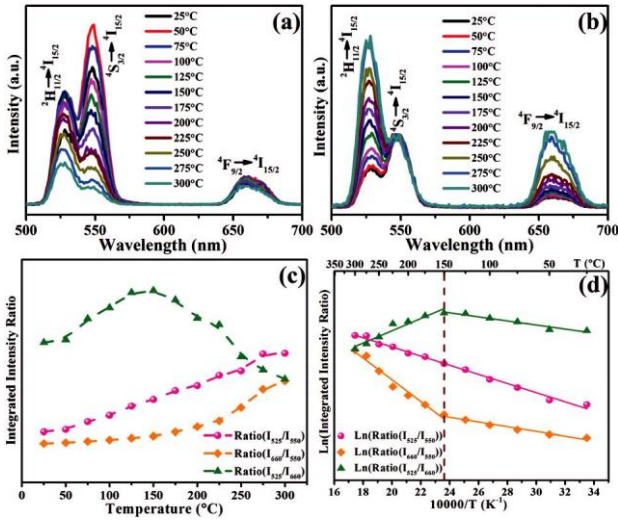


Fig. 2 (a) UC emission spectra of $\text{La}_{1.9}\text{Yb}_{0.06}\text{Er}_{0.04}\text{Mo}_{1.75}\text{W}_{0.25}\text{O}_9$ under excitation of a 980 nm laser beam (about B180 mW mm^{-2}) at various temperatures and (b) the same spectra with normalization at the 550 nm peak. (c) Variations in the integrated UC emission intensity ratios of $\text{La}_{1.9}\text{Yb}_{0.06}\text{Er}_{0.04}\text{Mo}_{1.75}\text{W}_{0.25}\text{O}_9$, i.e., ratio(I_{525}/I_{550}) (magenta ball), ratio(I_{660}/I_{550}) (orange square), and ratio(I_{525}/I_{660}) (cyan up-triangle) (the lines are to guide the eye), with temperature and (d) logarithmic plot of the intensity ratio of I_{525}/I_{550} ($\text{Ln}(\text{ratio}(I_{525}/I_{550}))$), I_{660}/I_{550} ($\text{Ln}(\text{ratio}(I_{660}/I_{550}))$) and I_{525}/I_{660} ($\text{Ln}(\text{ratio}(I_{525}/I_{660}))$) as a function of inverse absolute temperature of $\text{La}_{1.9}\text{Yb}_{0.06}\text{Er}_{0.04}\text{Mo}_{1.75}\text{W}_{0.25}\text{O}_9$. The lines are fitted.

which both the B525 nm peak and B660 nm peak intensities apparently increase.

The absolute emission intensities of lanthanide ions are greatly influenced by many factors, such as grain sizes, light-focused domain sizes, pumping power density, fluctuation of light source and spectrometer.^{4,33,34} Therefore, it should be more convincing to use the relative integrated intensity ratios of the three emission peaks of Er^{3+} (I_{525} , I_{550} and I_{660}) to evaluate the temperature effect on UC luminescence, as depicted in Fig. 2c. The intensity ratios of I_{525}/I_{550} and I_{525}/I_{660} monotonically increase with an increase in temperature, and the intensity ratio of I_{660}/I_{550} also increases but behaves differently above 150 IC. Owing to the small energy gap of about 800 cm^{-1} between the $^2\text{H}_{11/2}$ and $^4\text{S}_{3/2}$ levels, the $^2\text{H}_{11/2}$ level can be easily populated from the $^4\text{S}_{3/2}$ level through thermal activation, which leads to a variation in the $^2\text{H}_{11/2} - ^4\text{I}_{15/2}$ and $^4\text{S}_{3/2} - ^4\text{I}_{15/2}$ transitions of Er^{3+} at different temperatures.^{4,33,34} The intensity ratio versus temperature $\text{Ln B}/T$ plot should be linear, which is the basis of optical temperature sensing applications and can be understood by the following equation:

$$R = \frac{I_{525}}{I_{550}} \frac{N_{^2\text{H}_{11/2}}}{N_{^4\text{I}_{15/2}}} \frac{N_{^4\text{S}_{3/2}}}{N_{^4\text{I}_{15/2}}} \exp\left(-\frac{DE}{kT}\right) \quad (1)$$

where, R is the intensity ratio and I_{525} and I_{550} are the integrated intensities of the $^2\text{H}_{11/2} - ^4\text{I}_{15/2}$ and $^4\text{S}_{3/2} - ^4\text{I}_{15/2}$ emissions, respectively. $N(^2\text{H}_{11/2})$ and $N(^4\text{S}_{3/2})$ represent the population numbers of the $^2\text{H}_{11/2}$ and $^4\text{S}_{3/2}$ levels, respectively. DE is the energy gap between the $^2\text{H}_{11/2}$ and $^4\text{S}_{3/2}$ levels, k is the Boltzmann constant, T is the absolute temperature and C represents the

pre-exponential constant. Herein, the linear behavior is used as an internal reference to characterize the two other lognormal plots of UC emission intensity ratio, as depicted in Fig. 2d and 3a–c. It is obvious that there is an apparent break point at B150 IC in all the samples with different concentrations of W. The break point should have some relationship with short-range oxide-ion motion (jump), as evidenced in previous work.⁴ The oxide-ion jump (forming the anion-Frenkel defects) should be on a scale of a few angstroms in the crystal lattice, which could be sensed by the sensitive UC emissions of nearby lanthanide ions. Thus, the break point suggests that Er^{3+} experiences large chemical environmental variations when the temperature is above 150 IC, which is probably ascribed to the thermally-activated oxide-ion motion. To confirm this, AC impedance spectroscopy data of the samples were recorded as a reference for long-range oxide-ion motion. The permittivity value at 10^{-7} – $10^{-5} \text{ F cm}^{-1}$ of the electric double layers formed between electrodes can indicate long-range oxide-ion motion.³⁹ Fig. 3d–f present the permittivity of the $\text{La}_{1.9}\text{Yb}_{0.06}\text{Er}_{0.04}\text{Mo}_2 \times \text{W}_x\text{O}_9$ ($x = 0.25, 0.75$ and 1.25) ceramic pellets as a function of frequency at different temperatures. The $\text{La}_{1.9}\text{Yb}_{0.06}\text{Er}_{0.04}\text{Mo}_2 \times \text{W}_x\text{O}_9$ ($x = 0.25, 0.75$ and 1.25) ceramics all possess a permittivity of $\text{B}10^7 \text{ F cm}^{-1}$ at 300 IC. The large permittivities at low frequency are ascribed to the electric double layers between electrodes, which block the oxide-ion motion at a distance of B1 mm (the thickness of the ceramic samples).

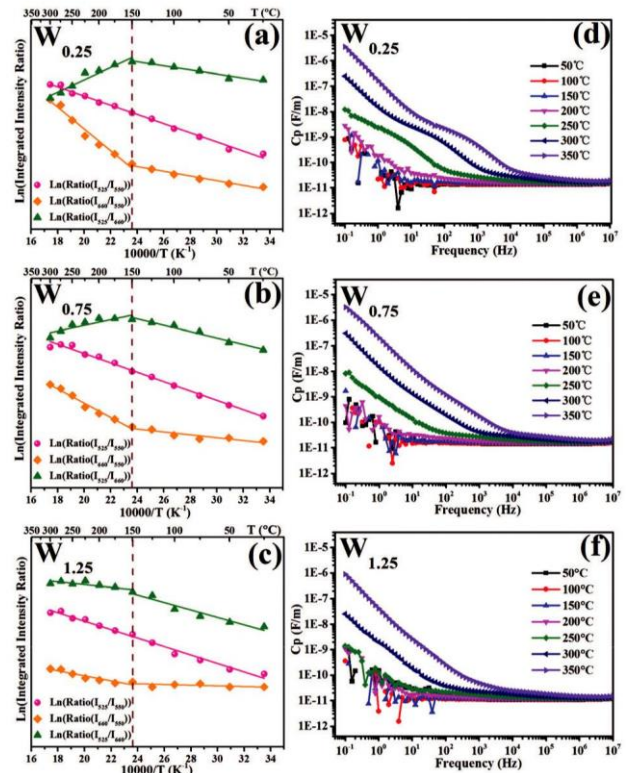


Fig. 3 (a–c) Lognormal plots of the intensity ratio of I_{525}/I_{550} ($\text{Ln}(\text{ratio}(I_{525}/I_{550}))$), I_{660}/I_{550} ($\text{Ln}(\text{ratio}(I_{660}/I_{550}))$) and I_{525}/I_{660} ($\text{Ln}(\text{ratio}(I_{525}/I_{660}))$) as a function of inverse absolute temperature of $\text{La}_{1.9}\text{Yb}_{0.06}\text{Er}_{0.04}\text{Mo}_2 \times \text{W}_x\text{O}_9$ ($x = 0.25, 0.75$ and 1.25). (d–f) Permittivity of the $\text{La}_{1.9}\text{Yb}_{0.06}\text{Er}_{0.04}\text{Mo}_2 \times \text{W}_x\text{O}_9$ ($x = 0.25, 0.75$ and 1.25) ceramic pellets as a function of frequency at different temperatures.

This distance should cover plenty of crystal grains (on the micrometer scale) and should be considered as long range. Associating the break points in the plots of $\ln B$ $1/T$ with permittivity variation, it can be inferred that there is a correlation between the break points and short-range oxide-ion motion.³⁹ This relationship is also proven by the case of LaGaO_3 derivatives with and without oxide-ion conduction, as depicted in Fig. S2 (ESI[†]). Actually, the neutron diffraction data for the $\text{La}_2\text{Mo}_2\text{O}_9$ derivatives in Fig. 4 gives further direct evidence of the oxide-ion jumps at 100–200 1C ^{22,32} since the light atom O in the crystal lattice contributes largely to the scattering of neutrons and equivalent isotropic temperature factors of O behave distinctly in this temperature range. Furthermore, the conductivity of the grain boundary is of the same magnitude or even higher than that of the grain, as shown in Fig. S1 (ESI[†]), which suggests that the amorphous grain boundary might have ionic conductivity. The amorphous phase (Fig. S3, ESI[†]) shows an analogous temperature-dependent UC behaviour in Fig. S4 (ESI[†]) when doped with $\text{Yb}^{3+}/\text{Er}^{3+}$. Actually, the higher conductive amorphous phase is also proven by recent research on $\text{La}_2\text{Mo}_2\text{O}_9$ nanowires with an amorphous surface.¹⁷

Fig. 5a presents plots of the slopes below and above the break points versus W contents of Fig. 3a–c, in which $\ln(R(I_{525}/I_{660}))$ and $\ln(R(I_{660}/I_{550}))$ show large variations in temperature above the break point (B150 1C), whereas there is slight change in temperature below the break point. This also manifests that the oxide-ion motion above 150 1C significantly influences the UC behaviors of Er^{3+} . The temperature-dependent grain conductivities of $\text{La}_{1.9}\text{Yb}_{0.06}\text{Er}_{0.04}\text{Mo}_2\text{W}_x\text{O}_9$ ($x = 0.25, 0.75$ and 1.25) are depicted in Fig. 5b. Herein, both electronic and ionic conductivity contribute to the sum value. Fitting the conductivity in the Arrhenius region gives the activation energy. It can be found that the conductivity declines with an increase in W content at a certain temperature, and the activation energy increases. DFT calculations on electronic structure may give some clues to these phenomena.

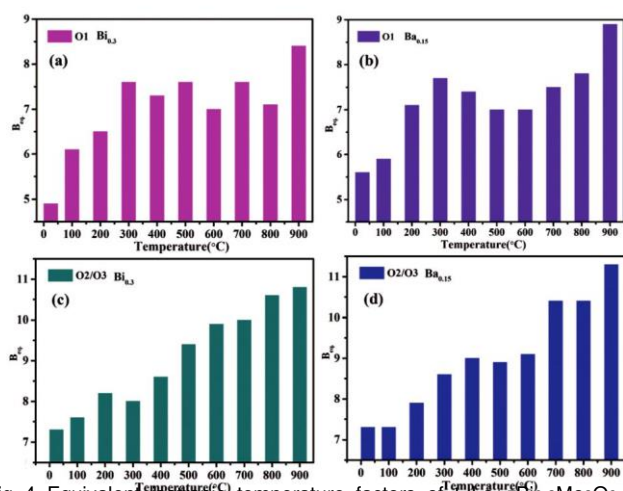


Fig. 4 Equivalent isotropic temperature factors of b- $\text{La}_{1.7}\text{Bi}_{0.3}\text{Mo}_2\text{O}_9$ (a) O1 and (c) O2/O3 and b- $\text{La}_{1.85}\text{Ba}_{0.15}\text{Mo}_2\text{O}_{8.925}$ (b) O1 and (d) O2/O3 (cubic space group $P2_13$, No. 198) from neutron powder diffraction data. (Data adopted from Chem. Mater., 2014, 26, 6838–6851 (ref. 20) and

Chem. Mater., 2011, 23, 1288–1298 (ref. 30).)

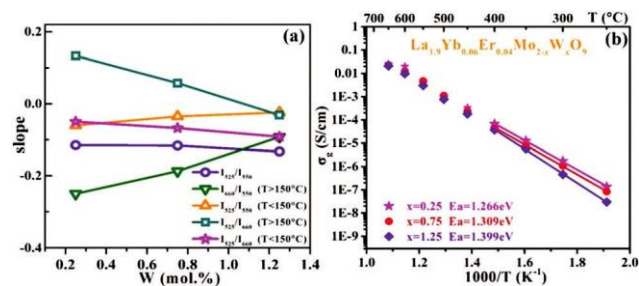


Fig. 5 (a) Variations in the slopes in lognormal plots of UC emission intensity ratio vs. temperature with different concentrations of $\text{La}_{1.9}\text{Yb}_{0.06}\text{Er}_{0.04}\text{Mo}_2\text{W}_x\text{O}_9$ ($x = 0.25, 0.75$ and 1.25). Below/above the temperature of break point, the lines are to guide the eye. (b) Temperature dependency of the conductivity measured in air on dense ceramic for different compositions of $\text{La}_{1.9}\text{Yb}_{0.06}\text{Er}_{0.04}\text{Mo}_2\text{W}_x\text{O}_9$ ($x = 0.25, 0.75$ and 1.25). The variation in the activation energy for different compositions is shown in the figure.

DFT calculations

It can be clearly seen in Table 1 that substitution of Mo by W has much lower formation energies compared with doping at the La site, which means that W doping can be easily accomplished without much difficulty. This could be attributed to the fact that their valence state is the same and ionic radius similar (difference less than 0.001 nm) based on the LPS concept of Lacorre.⁴⁰ This is consistent with the former research on W-doped $\text{La}_2\text{Mo}_2\text{O}_9$, which showed high compatibility with the lattice and high doping limits that can reach up to 80%; however, the ion conductivity showed no significant variation.^{41,42} The formation of a-Fr in W-doped $\text{La}_2\text{Mo}_2\text{O}_9$ has very distinct results in different positions. Since we only have limited models on W-doped $\text{La}_2\text{Mo}_2\text{O}_9$, based on the former research results, we believe that the model with a high formation energy of up to 4.992 eV could be a very special case and hard to realize in actual experiment.

The electronic properties can be shown through projected density of states (PDOS). All four patterns in Fig. 6 display similar results with a pair of symmetrical gap states pinned at the Fermi level (EF). This EF pinning effect arises from the Mo–O bond rather than any influence from W, which means that both the doping process and formation of an a-Fr pair do not impose strong effect on the electronic structure of the lattice and the material will remain insulating. The a-Fr is only related to ion conductivity and doping in $\text{La}_2\text{Mo}_2\text{O}_9$ mainly influences the stability of the conductive phase of $\text{La}_2\text{Mo}_2\text{O}_9$. This phenomenon suggests that $\text{La}_2\text{Mo}_2\text{O}_9$ can be considered as a pure ion conductor and its electronic properties will remain insulating which are difficult to alter.

Table 1 Formation energy of W doping in different positions and with a-Fr pair defects

Compound	Formation energy (eV)
$\text{La}_{1.5}\text{W}_{0.5}\text{Mo}_2\text{O}_9$	6.854
$\text{La}_2\text{Mo}_{1.5}\text{W}_{0.5}\text{O}_9$	0.709
$\text{La}_2\text{Mo}_{1.5}\text{W}_{0.5}\text{O}_9\text{-a-Fr}$	0.191

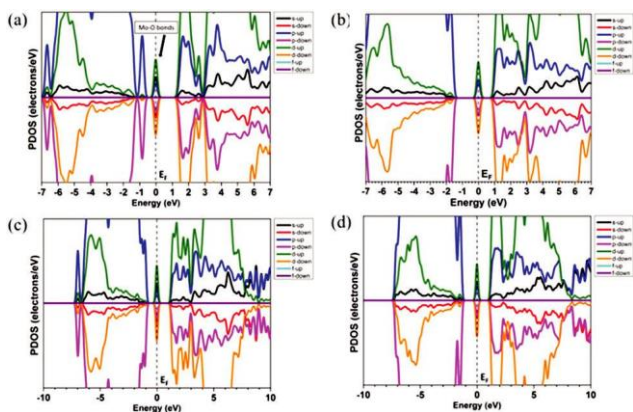


Fig. 6 (a) PDOS of the parent $\text{La}_2\text{Mo}_2\text{O}_9$, (b) PDOS of $\text{La}_2\text{Mo}_2\text{O}_9$ with an a-Fr pair, (c) PDOS of W-doped $\text{La}_2\text{Mo}_2\text{O}_9$ at Mo site and (d) PDOS of W-doped $\text{La}_2\text{Mo}_2\text{O}_9$ with an a-Fr pair.

Therefore, the variation in conductivity shown in Fig. 5b should be mainly due to the change in ion conduction. Considering the capacity of oxide-ion motion (permittivity) in Fig. 3a–c, the incorporation of W will increase the barrier of formation for new a-Fr defects, resulting in higher activation energy and lower ion conductivity at low temperature (0400 IC).

Conclusions

This research correlates the UC emission of Er^{3+} with the oxide-ion motion in b- $\text{La}_2(\text{Mo},\text{W})_2\text{O}_9$. Associating the break points in the plots of $\ln B$ 1/T with permittivity variation, the break points should be ascribed to short-range oxide-ion motion. Also, the behaviors (slopes) of the plots above the temperature of the break points reflect long-range oxide-ion motion. The incorporation of W will increase the barrier for the formation of new a-Fr defects, resulting in a higher activation energy and lower ion conductivity as unraveled by permittivity at low temperature and DFT calculations. This research allows an alternative optical approach to monitor the oxide-ion conductors employed in devices.

Conflicts of interest

There are no conflicts of interest to declare.

Acknowledgements

This work is financially joint supported by the NSFC (Grant No. 51472088, 51772104), the Tip-top Scientific and Technical Innovative Youth Talents of Guangdong special support pro-gram (2016TQ03C100) and the Guangdong Natural Science Funds for Distinguished Young Scholar (2014A030306009).

References

1 Y. H. Huang, R. I. Dass, Z. L. Xing and J. B. Goodenough, *Science*, 2006, 312, 254–257.

2 X. Kuang, M. A. Green, H. Niu, P. Zajdel, C. Dickinson, J. B. Claridge, L. Jantsky and M. J. Rosseinsky, *Nat. Mater.*, 2008, 7, 498–504.

3 P. Lacorre, F. Goutenoire, O. Bohnke, R. Retoux and Y. Laligant, *Nature*, 2000, 404, 856–858.

4 Y. Li, X. Jiang, F. Tao, Y. Yang, Q. Zhang and S. Ye, *J. Mater. Chem. C*, 2016, 4, 7286.

5 C. J. Hou, Y. D. Li, P. J. Wang, C. S. Liu, X. P. Wang, Q. F. Fang and D. Y. Sun, *Phys. Rev. B: Condens. Matter Mater. Phys.*, 2007, 76, 014104.

6 C. Tealdi, G. Chiodelli, L. Malavasi and G. Flor, *J. Mater. Chem.*, 2004, 14, 3553.

7 T. Paul and A. Ghosh, *J. Alloys Compd.*, 2014, 613, 146–152.

8 L. H. Fischer, G. S. Harms and O. S. Wolfbeis, *Angew. Chem., Int. Ed.*, 2011, 50, 4546–4551.

9 J. H. Hao, Y. Zhang and X. H. Wei, *Angew. Chem., Int. Ed.*, 2011, 50, 6876–6880.

10 S. Tanabe, T. Ohyagi, N. Soga and T. Hanada, *Phys. Rev. B: Condens. Matter Mater. Phys.*, 1992, 46, 3305–3310.

11 B. R. Judd, *Phys. Rev.*, 1962, 127, 750–761.

12 G. S. Ofelt, *J. Chem. Phys.*, 1962, 37, 511–520.

13 Z. Yu, Z. Xia, E. Liu and Q. Liu, *Dalton Trans.*, 2016, 45, 16240–16245.

14 Z. Xia and K. R. Poepfelmeier, *Acc. Chem. Res.*, 2017, 50, 1222–1230.

15 D. Marrero-Lo'pez, P. Nu'n'ez, M. Abril, V. Lavi'n, U. R. Rodr'iguez-Mendoza and V. D. Rodr'iguez, *J. Non-Cryst. Solids*, 2004, 345–346, 377–381.

16 G. Corbel, P. Durand and P. Lacorre, *J. Solid State Chem.*, 2009, 182, 1009–1016.

17 W. Liu, W. Pan, J. Luo, A. Godfrey, G. Ou, H. Wu and W. Zhang, *Nat. Commun.*, 2015, 6, 8.

18 M. Y. Dan, M. Q. Cheng, H. Gao, H. Zheng and C. Q. Feng, *J. Nanosci. Nanotechnol.*, 2014, 14, 2395–2399.

19 I. R. Evans, J. A. K. Howard and J. S. O. Evans, *Chem. Mater.*, 2005, 17, 4074–4077.

20 T. Paul and A. Ghosh, *J. Appl. Phys.*, 2013, 114, 164101.

21 X. P. Wang and Q. F. Fang, *Phys. Rev. B: Condens. Matter Mater. Phys.*, 2002, 65, 064304.

22 G. Corbel, A. Selmi, E. Suard and P. Lacorre, *Chem. Mater.*, 2014, 26, 6838–6851.

23 V. Voronkova, E. Kharitonova and A. Krasilnikova, *Phys. Status Solidi A*, 2009, 206, 2564–2568.

24 L. Haoran, W. Chang-An and M. A. White, *J. Am. Ceram. Soc.*, 2015, 98, 1385–1388.

25 M. Guzik, M. Bieza, E. Tomaszewicz, Y. Guyot and G. Boulon, *Z. Naturforsch., B: J. Chem. Sci.*, 2014, 69, 193–204.

26 M. Guzik, M. Bieza, E. Tomaszewicz, Y. Guyot, E. Zych and G. Boulon, *Opt. Mater.*, 2015, 41, 21–31.

27 F. Goutenoire, O. Isnard, E. Suard, O. Bohnke, Y. Laligant, R. Retoux and P. Lacorre, *J. Mater. Chem.*, 2001, 11, 119–124.

28 J. P. Fournier, J. Fournier and R. Kohlmuller, *Bull. Soc. Chim. Fr.*, 1970, 4277–4283.

29 Z. Y. Lu, X. M. Li and J. Q. Wu, *J. Am. Ceram. Soc.*, 2012, 95, 476–479.

- 30 S. A. Hayward and S. A. T. Redfern, *J. Phys.: Condens. Matter*, 2004, 16, 3571–3583.
- 31 X. P. Wang, D. Li, Q. F. Fang, Z. J. Cheng, G. Corbel and P. Lacorre, *Appl. Phys. Lett.*, 2006, 89, 021904.
- 32 G. I. Corbel, E. Suard and P. Lacorre, *Chem. Mater.*, 2011, 23, 1288–1298.
- 33 H. Berthou and C. K. Jorgensen, *Opt. Lett.*, 1990, 15, 1100–1102.
- 34 V. K. Rai, *Appl. Phys. B: Lasers Opt.*, 2007, 88, 297–303. 41 D. Marrero-López, J. Canales-Vázquez, W. Zhou, J. T. S. Irvine and P. Núñez, *J. Solid State Chem.*, 2006, 179, 278–288.
- 35 S. Du, X. Ma, Q. Qiang, G. Zhang and Y. Wang, *Phys. Chem. Chem. Phys.*, 2016, 18, 26894–26899.
- 36 P. Du, L. H. Luo, W. P. Li, Q. Y. Yue and H. B. Chen, *Appl. Phys. Lett.*, 2014, 104, 152902.
- 37 X. Yi, Z. T. Chen, S. Ye, Y. Li, E. H. Song and Q. Y. Zhang, *RSC Adv.*, 2015, 5, 49680–49687.
- 38 X. N. Chai, J. Li, X. S. Wang, Y. X. Li and X. Yao, *Opt. Express*, 2016, 24, 22438–22447.
- 39 J. T. S. Irvine, D. C. Sinclair and A. R. West, *Adv. Mater.*, 1990, 2, 132–138.
- 40 P. Lacorre, *Solid State Sci.*, 2000, 2, 755–758.
- 42 L. Baque, J. Vega-Castillo, S. Georges, A. Caneiro and E. Djurado, *Ionics*, 2013, 19, 1761–1774.